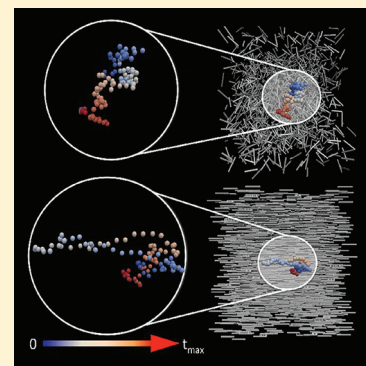


# Diffusion of a Spherical Probe through Static Nematogens: Effect of Increasing Geometric Anisotropy and Long-Range Structure

Ashley K. Tucker and Rigoberto Hernandez\*

Center for Computational Molecular Science and Technology, School of Chemistry and Biochemistry, Georgia Institute of Technology, Atlanta, Georgia

**ABSTRACT:** Diffusional behavior of a spherical probe through static nematogens (or needles) is probed via molecular dynamics simulations. The needles are modeled as spherocylinders and are arranged in idealized limits of an isotropic phase and a slowly quenched nematic mesh. The spherical probe exhibits superdiffusive motion through both the isotropic and nematic scatterer configurations. The superdiffusive behavior results from directional collisions between the spherical probe and the static nematogens. Velocity autocorrelation functions show long time correlations caused by directionality of transport due to the geometric anisotropy of the scatterers; however, glassy behavior exhibited by the tracer is observed when the scatterers are sufficiently long, leading to a downturn in the diffusion coefficients. Diffusion through the nematic configuration shows anisotropic diffusion with preferential motion occurring along the orientational director by way of effective channels formed by the long-range orientational order of the aligned nematogens.



## I. INTRODUCTION

Many systems exhibit anisotropic diffusion caused by geometric or spatial anisotropy. One such class of systems typically includes a probe or solute diffusing through fixed scatterers arranged in an ordered array or within liquid crystalline phases.<sup>1–6</sup> A simple model exhibiting anisotropic diffusion can be constructed from a variant of the Lorentz model in which the static scatterers are fixed spherically capped needles (with length  $L + d$  and a nontrivial width  $d$ ) while a spherical probe is allowed to freely translate through the resulting mesh. The ability of the probe to diffuse through the scattering needles depends upon the density, the aspect ratio  $L/d$  and the long-range orientation of the scatterers. As the aspect ratio of the needles goes to 0 (with  $L$  approaching zero or  $d$  approaching infinity), the system dynamics simply reduces to that of a spherical probe translating through static spheres. When the aspect ratio of a static needle is increased, the geometric anisotropy as well as its ability to exhibit long-range order leads to complex behavior in the dynamics of the spherical solute.

Theoretical and experimental work performed on systems containing a spherical probe moving through geometrically anisotropic particles include fibrous filaments,<sup>4,5</sup> suspensions of spherocylindrical colloids or ellipsoids,<sup>1</sup> and lyotropic liquid crystals of *fd* virus.<sup>7–9</sup> Silica tracer beads with large radii diffusing through colloidal silica rods have been seen experimentally to depend on rod density.<sup>5</sup> When the density of rods is low, the diffusion of the bead is determined by the fluid in which the rods and beads are suspended. Upon increasing rod density to the point where caging effects begin to dominate, the dynamics depend on the tracer size relative to the size of the mesh network formed by the caged rods.<sup>5</sup> Numerical studies have also shown similar results; excluded volume and spherical contact with rods dictate the dynamical behavior.<sup>4</sup> Theoretical and experimental work on a

spherical tracer (apoferritin) in *fd* virus show similar hydrodynamic considerations with respect to tracer size.<sup>7–9</sup>

Bagchi and co-workers<sup>1</sup> developed a theory to describe the diffusion of a spherical tracer through a liquid crystal consisting of ellipsoid particles near the isotropic–nematic phase transition. They found that the dynamics of the tracer becomes increasingly anisotropic with increasing long-range order in the ellipsoidal particles and that the transition was strongly affected by the tracer radius.<sup>1</sup> In these results, the dynamical effect of changing the geometric anisotropy of liquid crystal particles is not as well described as the effects of changing the dimensions of the probe. It is notable that a reduced-dimensional (very much simplified) model of a chemical reaction solvated by driven nematogens did indicate the possibility for anisotropic effects due to the driving frequency.<sup>10</sup>

Much work has been performed to study Lorentz models, that is, systems in which a probe particle diffuses through a series of static scatterers with a variety of geometric structures for both the solute and the static scatterers.<sup>11–21</sup> Variants of these systems have been widely studied and have provided insight into diffusive behavior in a number of more complex systems.<sup>11,13,20–24</sup> Lorentz models have been utilized to recreate diffusion in a network of polymers<sup>25</sup> as well as to observe nontrivial scatterer density dependence.<sup>13,20,22,24</sup> The dynamics of the probe within Lorentz models can exhibit nonstationary behavior.<sup>26–28</sup> Lorentz model systems also have been shown to exhibit interesting long time tails in the mean square displacement (MSD) and the velocity autocorrelation function (VACF), as well as

Received: August 1, 2011

Revised: December 2, 2011

Published: December 08, 2011

nonexponential decay of the VACF when the scatterer density is large.<sup>11–20</sup>

Previous work on Lorentz models composed of spherical scatterers with a structureless point particle probe have displayed unexpected density dependence in both two and three dimensions.<sup>11,12</sup> The probe particle exhibits expected diffusive behavior until a critical scatterer density is reached. Thereafter, it begins to exhibit subdiffusive behavior.<sup>11</sup> Höfling et al.<sup>13</sup> also found distinct regimes in the dynamics of a freely rotating and translating needle diffusing through a two-dimensional Lorentz model of structureless point scatterers. Variation in the density of scatterers as well as in the needle width can be used to tune the behavior with respect to different types of motion across three different regimes: the expected Enskog diffusion at low densities, reptative diffusion exhibited by entangled polymers, and glassy motion in which the needle particle is essentially trapped.<sup>13,20,21</sup> In the case of spherical scatterers, there is also significant precedent<sup>22–24</sup> showing that the presumed structure of the scatterers can play a dramatic role in the diffusion coefficients of the probe. Indeed, some of the differences seen in the diffusive dynamics of a needle through spherical scatterers by various groups<sup>11,13,20,21</sup> can be attributed in part to the varying choices of scatterer configurations they employed.

In this article, we focus on the dynamics of a spherical probe diffusing through a three-dimensional Lorentz model of rodlike scatterers. The rodlike (or needle) scatterers can be oriented isotropically or directed along a specified orientation, such as in a nematic phase. Thus, this model system can possess both geometric and spatial anisotropy. Such systems can form liquid crystal phases under appropriate conditions, perhaps leading to preferred directions of transport. The objective of this work is to determine whether this anisotropy can lead to unusual diffusive dynamics of any kind, in particular, one that is preferentially directed.

To study the effects due to varying geometric and spatial anisotropy in the collective structure of the scatterers, two idealized limiting cases are considered: (i) randomized placement of the center of mass and orientation of the Lorentz needles forming a static isotropic phase, and (ii) randomized placement of the needles' center of mass positions but with their orientations taken to be fixed along the  $x$ -axis of the simulation box, leading to a specified long-range orientational order (as in a static nematic phase that has been quenched slowly enough to elicit perfect alignment). Thus, this model incorporates the effect of geometric anisotropy of each scatterer and collective long-range order of the scatterers on the resulting dynamics of a spherical probe. As stated in the first paragraph, the static scatterers are modeled as spherocylindrical particles in which the geometric anisotropy is varied by changing the length,  $L$ , of the cylindrical portion of the spherocylinder relative to the diameter of the hemisphere cap,  $d$ . Aspect ratios,  $L/d$ , range from 1 to 10. The simulations were predominantly performed for scatterers with a monodisperse distribution of fixed (and equal) polymer lengths. Such a simplification was seen to be warranted because the diffusion coefficients did not change appreciably when the scatterer lengths were distributed according to a Gaussian distribution with widths up to one-tenth the size of  $L$ .

The systems of interest referenced above contain anisotropic particles where  $L/d$  ranges from  $\sim 3$  to 10 for molecular dynamics simulations of liquid crystalline molecules to  $\sim 300$  for systems containing  $fd$  virus. For spherocylinders, previous work has shown that liquid crystal phases are accessed when  $L/d \geq 3$ .<sup>29</sup> Section III provides evidence that the onset of glassy behavior in

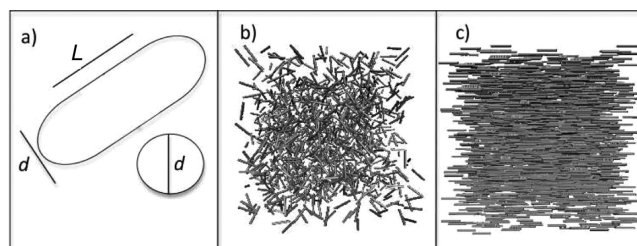


**Figure 1.** Panel a illustrates the aspect ratio ( $L/d$ ) of the static nematogens with respect to the spherical tracer diameter  $d$ . The middle panel, b, illustrates one snapshot of the isotropically oriented nematogens. Panel c illustrates the nematically oriented nematogens with spherocylinders aligned along the  $x$ -axis. For fixed aspect ratio, the length of the cylindrical portion,  $L$ , is varied, thereby effectively changing the occupied volume fraction.

the probe dynamics is correlated with density and the degree of long-range order. In turn, an increase in the needles' long-range order staves off the onset of the probe's glassy dynamics. Thus, the density of scatterers as well as the orientational order affects the dynamics of the probe.

## II. MODEL AND SIMULATION DETAILS

The Lorentz model studied in this work consists of a three-dimensional static array of spherocylindrical scatterers; namely, needles. The center of mass of each scatterer is placed randomly throughout the simulation box. The absolute and relative orientations of the needles are chosen according to one of two algorithms corresponding to either isotropic or nematic structure. Isotropically oriented particles are obtained by randomly rotating the spherocylinders while preventing overlaps. In the nematic case, the needles are aligned along a director with perfect fidelity. This choice of preparation does not correspond to a fast quench of an equilibrium configuration of a nematic phase because that would evidently exhibit a distribution of orientations around the director. It corresponds, instead, to a slow-enough quench of the nematic phase experiencing a strong-enough field from the director as to ensure that there is a nearly infinitely narrow distribution of orientations. A visual representation of each system is provided in Figure 1.

A spherical tracer diffusing through the Lorentz scatterers is propagated according to Newtonian mechanics. The interparticle forces between the tracer and the fixed needles is specified by a "hard-sphere" potential that is either constant (and set to zero) when the corresponding solid structures do not overlap or infinite otherwise. Each simulation is carried out at constant energy with a value corresponding to an effective temperature, 300 K, as computed from the initial velocities of the probe. Periodic boundaries are employed in all directions, and the overall magnitude of the tracer's velocity vector remains constant because the tracer/scatterer interactions are governed via a hard potential. The spherical tracer's surface is smooth; thus, its rotation was not considered. Scatterer volume fraction was controlled by varying the length of each spherocylinder and not by changing the number of scatterers.

Once the spherocylinder scatterers are placed within an appropriate phase, they are frozen in place. The tracer particle is allowed to diffuse through the system. Integration of the equations of motion for this model is carried out using an in-house Fortran code. The sphere is propagated as a free particle

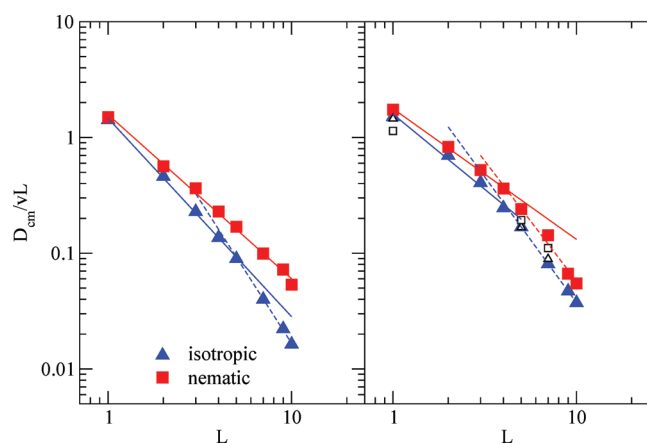


**Figure 2.** The diffusion coefficients for the nematic (orange squares) and isotropic (blue triangles) realization of the mesh with respect to the needle cylinder length. The right panel shows data for scatterer width  $\sigma = 0.5$  nm, and the left, for  $\sigma = 0.7$  nm. The volume fraction increases with increasing aspect ratio. Open symbols in the right panel—squares for nematic and triangles for isotropic—illustrate the diffusion coefficients when the scatterer lengths are distributed according to a Gaussian distribution with a width that is 10% of the corresponding average  $L$ . Dotted lines show power-law fits to the diffusion coefficients and help guide the eye to where the critical aspect ratio gives rise to entrapment.

between collisions according to the well-known expression

$$\mathbf{r}(t + \tau) = \mathbf{r}(t) + \mathbf{v}(t)\tau \quad (1)$$

where  $\mathbf{v}$  is the linear velocity. The time-step,  $\tau$ , is chosen to be a constant value of 0.1 ps for the ease of collecting data at constant time intervals. In the specific systems considered here for a given finite sized periodic box, this time step is short enough that usually no collisions or, at most, one rare such collision ever takes place during a time step.

Particle collisions are detected by determining the closest point between the scatterer and the spherical tracer. Once this point is determined, the relative velocity of this point is set to equal that of the spherical tracer. The collision normal is defined, and the relative normal velocity is determined by

$$\mathbf{v}_{\text{rel}} \cdot \mathbf{n} = \mathbf{v}(t) \cdot \mathbf{n} \quad (2)$$

where  $\mathbf{v}_{\text{rel}}$  is the relative velocity along the collision normal,  $\mathbf{v}$  is the velocity of the spherical particle, and  $\mathbf{n}$  is the collision normal. If  $\mathbf{v}_{\text{rel}}$  is positive, then the spherical tracer is moving away from the scatterer; if it is negative, then the particles are colliding. Postcollision velocities are determined by

$$\mathbf{v}_f = \mathbf{v}_i + \frac{j}{m} \mathbf{n} \quad (3)$$

where  $\mathbf{v}_f$  is the postcollisional tracer velocity,  $\mathbf{v}_i$  is the precollisional velocity,  $j$  is the momentum of the collision,  $\mathbf{n}$  is the collision normal, and the mass of the tracer is  $m$ . The momentum of the collision is defined as

$$j = -2m \left( \frac{\mathbf{v}_{\text{rel}} \cdot \mathbf{n}}{\mathbf{n} \cdot \mathbf{n}} \right) \quad (4)$$

where the relative velocity,  $\mathbf{v}_{\text{rel}}$ , is determined from eq 2.

The effect of variations in the geometrical anisotropy is considered as a function of variations in the scatterer aspect

ratio. The length of the cylindrical portion of the scatterers is varied while the particle density and diameter were held constant. The box size is taken to be large enough—at least 3 times the scattering length  $L$ —so as to ensure that the observed dynamics are converged and not affected by spurious correlations. Results are provided for scatterer densities that ultimately result in diminished diffusive (i.e., glassy) behavior when the scatterer aspect ratio is very large. The results are determined for two needle widths,  $\sigma = d/2$ ,  $\sigma = 0.5$  nm and  $\sigma = 0.7$  nm. Both needle widths resulted in glassy behavior of the probe when the volume fraction of the scatterers was high and the scatterers were arranged isotropically. Glassy probe dynamics was observed only in the thicker needles when they were ordered in a nematic phase.

### III. RESULTS AND DISCUSSION

This work aims to elucidate the dynamical behavior of a spherical probe diffusing through a static unconnected mesh of needles. Nontrivial behavior is expected for dense meshes in which the scatterer density is large enough for the probe to experience glassy behavior and, hence, is the regime studied here. Trapping behavior in these systems is effected by the geometry; the probe particle is trapped inside a cage of static scatterers, and it is not trapped by kinetic arrest, as seen in other glassy systems. The dynamics of a spherical tracer moving through the isotropic and nematic mesh has been simulated at several different scatterer aspect ratios and mesh densities. At a relatively low number density,  $\rho = 0.05$ , the mesh is seen to induce entrapment when the aspect ratio is large (and hence, the mesh becomes nearly space-filling). Two needle widths are studied,  $\sigma = 0.5$  nm and  $\sigma = 0.7$  nm. In the case of the needle width of  $\sigma = 0.5$  nm, entrapment of the probe is observed in the isotropic case only. The thicker needle width,  $\sigma = 0.7$  nm, was selected because it was seen to be large enough to effect trapping in the nematic meshes.

The diffusion coefficients for both the isotropic and nematic realizations of needles at the two selected needle widths are shown in Figure 2. For simplicity, most of the results reported here and elsewhere in this article have been performed on environments with monodisperse lengths fixed at  $L$ . In Figure 2, the diffusion coefficients for polydisperse needles with their lengths taken from a Gaussian distribution with width given by  $L/10$  are also shown for a few values of  $L$ . The diffusion coefficients are similar to the monodisperse case, indicating that the results are relatively insensitive to such a distribution. The volume fraction of the static needles depends upon both the needle width and length; thus, increased trapping for thicker needles is observed. The diffusion coefficients are shown in reduced dimensions relative to the average velocity,  $v$ , and the length of the cylindrical portion of the nematogen,  $L$ . All of the simulations have been performed at a constant temperature corresponding to an average rms velocity of  $\sim 0.06$  nm/ps.

Diffusion coefficients for the nematic phase are systematically larger than those for the isotropic phase. The difference in the diffusion coefficients becomes more prominent as the aspect ratio increases. This behavior is due to geometric anisotropy in concert with long-range order (spatial anisotropy), causing a preferred direction of transport. The orientation of the scatterers in concert with their geometric anisotropy results in channels in the nematic mesh through which the probe can easily diffuse. Thus, the spherical probe travels preferentially along the nematic director. The reduced number of reflective collisions in these



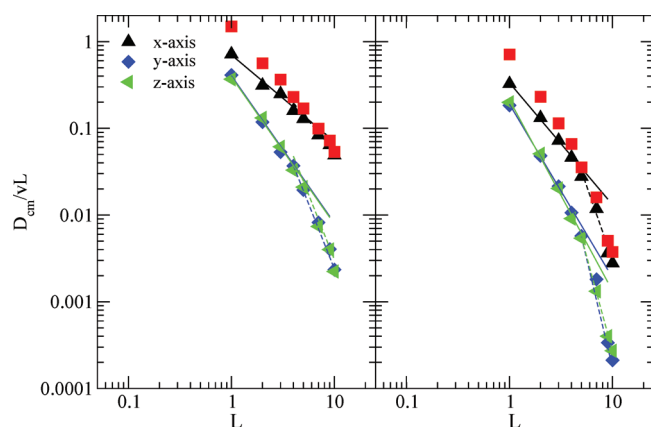


**Figure 3.** The diffusion coefficients in the nematic realizations of mesh for the thin needles (left) and thick needles (right) in the nematic direction,  $x$ -axis (black triangles) and the directions perpendicular (blue diamonds and green triangles). The overall diffusion coefficients are given by the red squares.

channels results in an overall increase in probe diffusion. A downturn in the diffusion coefficients is observed when the scatterer aspect ratio is high enough to induce glassy entrapment of the probe particle. On the other hand, the channels in the nematic mesh caused by the geometric anisotropy and long-range order help to stave off the entrapment for larger scatterer aspect ratios, where little entrapment is observed in the thinnest needles.

In the nematic case, the directed diffusion coefficients along the direction of needle alignment and perpendicular to the direction of alignment can be obtained separately. The respective diffusion coefficients provided in Figure 3 illustrate the role that the needle width plays in producing entrapment. As the volume fraction is increased by increasing the needle width, entrapment in the direction of nematic alignment is observed. This is due to the overall decrease in the size of the channels produced by the thicker needles relative to the thinner needles. Indeed, the average distance between scatterers for  $L = 7 \text{ Å}$  and  $\sigma = 0.5$  is  $3.6 \text{ Å}$ , but it is only  $3.3 \text{ Å}$  for  $\sigma = 0.7$  and  $L = 7 \text{ Å}$ .

The diffusion coefficients for the isotropic and nematic realizations of a spherical probe diffusing through a mesh of needles are compared in Figure 4 to the reverse case<sup>21</sup> in which a needle is allowed to diffuse through spherical scatterers. In both cases, the needles are taken to have a finite width equal to 1 nm. The diffusion coefficients are normalized by the geometric parameters of the needles in each model. The reported volume fractions correspond to the total volume fraction occupied by solvent and solute. Consequently, a larger number density of spherical scatterers is required to match the corresponding volume fraction of the static needles. (The volume fraction of the static needles depends on the needle width and length used, whereas for the stationary spherical scatterers, the volume fraction depends only upon the diameter of the spheres.) Both the diffusion of the asymmetric and spherical probe through the isotropic realization of the needle mesh and static spheres, respectively, exhibit a transition to geometric trapping with increasing volume fraction. The trapping of the needle—that is, the asymmetric probe—seems to be more severe than that experienced by the spherical probe in static needles. The diffusion of the spherical probe through the static needles is greatest when there is no entrapment, as illustrated in the case when the

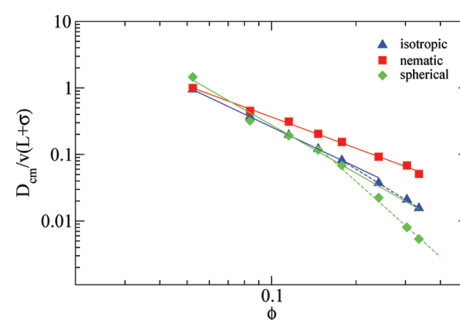


**Figure 4.** The diffusion coefficients for the nematic (orange squares), isotropic (blue triangles), and for a 3-dimensional needle in spherical scatterers (green diamonds) with respect to volume fraction. Power-law fits are provided to guide the eye to transitions to entrapment. The slopes of these lines correspond to the exponents in the power-law behavior. The observed exponents in the low-density regime for the spherical, nematic needle and isotropic needle scatterers are  $-2$ ,  $-1.6$ , and  $-2$ , respectively. The trapping transition was observed clearly only in the case of spherical and isotropic needle scatterers, for which the exponents are  $-4$  and  $-2.6$ , respectively.

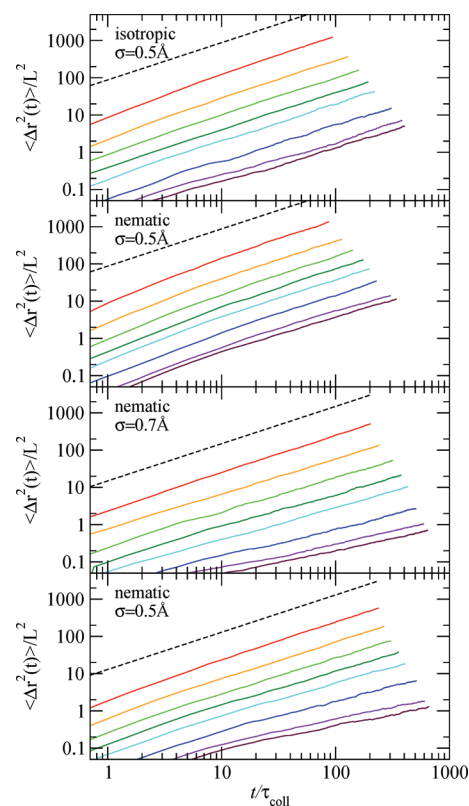


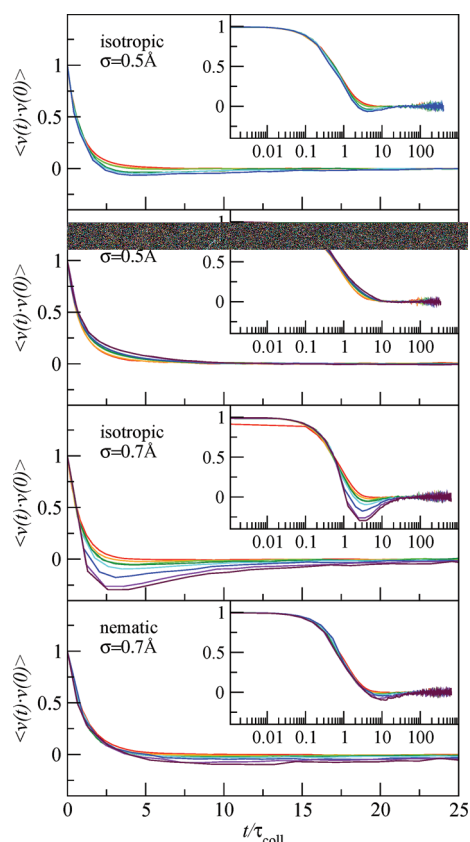
**Figure 5.** MSD as a function of time is shown for varying scatterer aspect ratios at two scatterer widths. The top two and bottom two panels show the data when the scatterers have a width  $\sigma = 0.5 \text{ nm}$  and  $\sigma = 0.7 \text{ nm}$ , respectively. The aspect ratio increases from 1 to 10 as the curves progress from red to purple. The dotted black lines indicate diffusive behavior.  $\langle r^2 \rangle \sim t$ , for reference.

spherical probe diffuses through a nematic mesh. Indeed, the trapping transition for this case was not seen over the observed range of volume fractions.

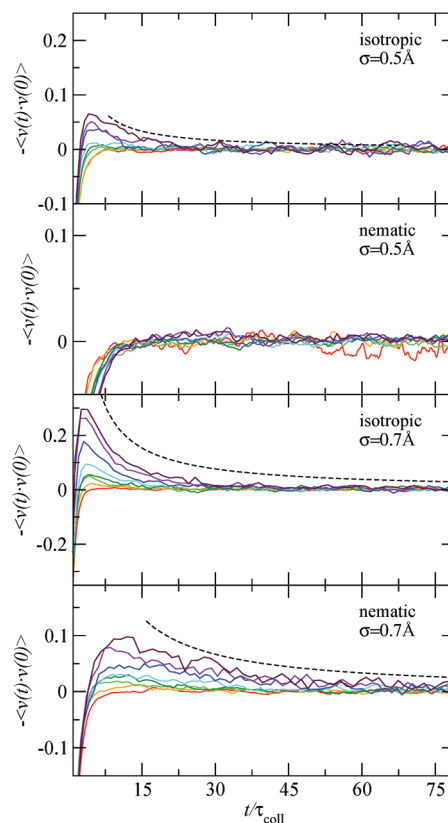
The panels in Figure 5 display the MSDs of a spherical probe diffusing through isotropic and nematic needle meshes scaled by

**Table 1.** Collision Times (ps) for Each Length of Needle, Orientation of the Mesh and Scatterer Width

$L$	$\sigma = 0.5$ nm		$\sigma = 0.7$ nm	
	isotropic	nematic	isotropic	nematic
1	106	113	49.3	41.9
2	77.6	88.2	41.0	37.3
3	62.4	70.5	31.4	32.5
4	51.5	56.9	26.5	27.9
5	45.1	50.3	23.0	24.5
7	32.2	43.7	19.5	19.4
9	26.1	32.8	16.7	16.4
10	24.6	29.2	15.4	15.1

**Figure 6.** The VACF as a function of time is shown for various scatterer aspect ratios at two scatterer widths. The top two and bottom two panels show the data when the scatterers have a width  $\sigma = 0.5$  nm and  $\sigma = 0.7$  nm, respectively. The aspect ratio increases from 1 to 10 as the curves progress from red to purple. The insets provide the VACFs on a semilog scale. Isotropic realizations of the mesh show slight negative correlations when the aspect ratio is large enough for direction reversing collision to dominate. Both phases and needle widths collapse reasonably well onto a single curve when normalized by the observed collision times listed in Table 1.

the square of the length,  $L$ , of the cylindrical portion of the needle scatterers. In both meshes, the probe's behavior transitions from superdiffusive at short times to diffusive motion at intermediate times. This transition is due to the nonspherically symmetric nature of the scatterers. The long cylindrical portion of each scatterer allows for directional collisions that do not result in frequent reflections of the probe particle. In the isotropic mesh,

**Figure 7.** The decay in the negative anticorrelations of the VACFs are highlighted through plots of the negative of the VACF shown here. The panels and symbols correspond to those in Figure 6 except for the dashed curve. The latter indicates a power-law fit describing the upper bound of the decay of the long-time tails as proportional to  $t^{-1}$ .

more direction-reversing collisions occur, leading to more reflections of the spherical probe. Thus, the transition to diffusive and subdiffusive behavior occurs at shorter times compared with the corresponding transitions observed in the nematic phase. When the aspect ratio is long enough to induce entrapment, subdiffusive dynamics is observed. A transition from diffusive motion to a subdiffusive plateau is observed for larger-aspect ratios in both the isotropic and nematic realizations of the needle mesh at the thicker needle width (0.7 nm). Figure 5 also indicates that enhanced mobility caused by channels in the nematic phase leads to larger distances covered by the spherical probe. The probe dynamics is seen to be more sensitive to volume fraction in the isotropic mesh than in the nematic mesh.

The VACFs for the diffusing probe are shown in Figure 6. The isotropic mesh gives rise to VACFs that depend weakly on the aspect ratios for low ratios. However, as the aspect ratio is increased, the spherical probe becomes trapped, and anticorrelations are observed. The needle length at which the backscattering begins to occur is also the point at which the diffusion coefficients calculated from the mean-square displacement begin to show trapping behavior. This is due to an increase in collisions, resulting in direction reversals of the spherical probe in the isotropic phase versus that in the nematic phase.

The anticorrelations occur around the critical aspect ratio in which entrapment begins. The VACFs for the nematic realizations appear to be much less influenced by the scatterer width. The anticorrelations in the VACFs are shown in greater detail in

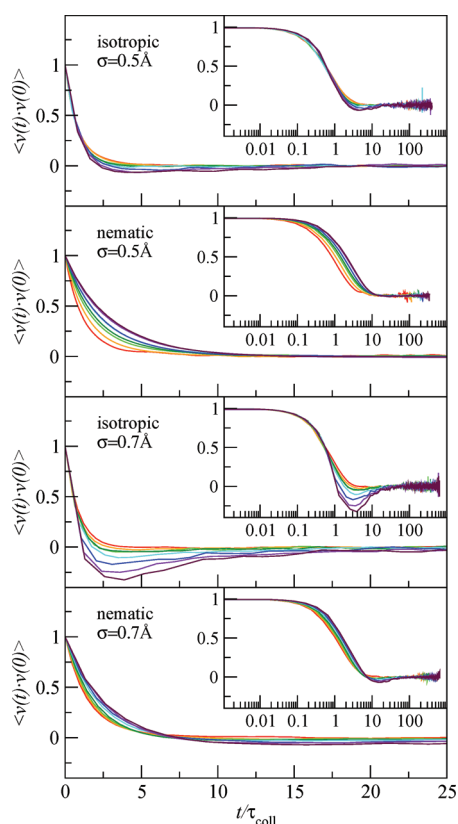


**Figure 8.** The VACF is shown along the nematic director ( $x$ -axis) for various aspect ratios. The panels and symbols correspond to those in Figure 7. The isotropic VACFs collapse reasonably well onto a single curve when normalized by collision time  $\tau_{\text{coll}}$ .

Figure 7 by taking the negative of the VACF and plotting the data over a longer time domain. The data indicate that upon trapping of the probe, long, negative time tails emerge. The observed negative time tails are bounded by the power-law behavior with an exponent of  $\sim -1$  for both the isotropic and nematic mesh when  $\sigma = 0.7$  nm. When the needle width is smaller,  $\sigma = 0.5$  nm, long time tails are observed only in the isotropic phase to be bounded by a power-law with an exponent near  $-1$ .

To observe the anisotropy of the dynamics of the spherical probe, the VACFs along the nematic director—the  $x$ -axis—are shown in Figure 8 for both static needle meshes and both needle widths. In the isotropic mesh, the VACFs collapse reasonably well when normalized by the collision times. Both data for the isotropic phase show an increase in anticorrelations as the needle length is increased. It is important to note that the VACFs along the perpendicular directions are almost identical for both needle widths in the isotropic mesh. The aspect ratio where these anticorrelations become prevalent is comparable to the needle lengths where entrapment begins to occur. The correlations in the velocity along the nematic director for the nematic phase show an increase in correlation as the needle length is increased for both needle widths. This is due to the increase in directional collisions caused by the effective tubes created by the long-range order of the system. In the nematic phase with the largest needle width, anticorrelations are observed when the needle is sufficiently long to induce geometric entrapment. The VACFs along the perpendicular directions decay more quickly than those along

the director. They also show anticorrelations at smaller aspect ratios, further indicating the formation of effective tubes in which the probe traverses.

#### IV. CONCLUSIONS

This work has investigated the overall aspect ratio dependence of the diffusion of a spherical probe in a mesh of static needles of varying long-range order. The orientational order of the geometrically anisotropic rods results in larger diffusion coefficients due to the effective channels or tubes created through which the particle diffuses. This result in qualitative agreement with the work of Kim et al.,<sup>30</sup> who found that the excluded volume effect drastically impacts the diffusion of a resulting Brownian particle through a porous media. These systems exhibit a crossover from superdiffusive to diffusive motion, as was seen earlier in the diffusion of needles through static Lorentz scatterers.<sup>13,20,31</sup>

In the dynamics of a probe through the static mesh, the density of the mesh affects the crossover more strongly when the mesh is isotropic than when it is nematic. As the aspect ratio of the needles is increased, evidence of more severe trapping in the isotropic mesh is displayed in both the MSD's—as seen in the plateaus that emerge with respect to aspect ratio—and in the VACFs along the nematic director, as seen through anticorrelations in the VACFs. As the probe becomes trapped with increasing scatterer length and width, we observe the appearance of anticorrelations and negative long time tails.

We also investigated the functional form of the negative long time tails due to the backscattering of the probe. The negative long-time tails are bounded by a power-law decay with an exponent  $\sim -1$ . The nematic mesh did not give rise to a trapping regime for the small needle widths, but did exhibit trapping when  $\sigma = 0.7$  nm. Enhanced transport was also seen for the spherical probe in the nematic mesh due to the long-range order and geometric anisotropy of the particle.

Although seemingly simple, the numerical propagation of a spherical probe diffusing through a static array of scatterers presented several computational challenges. It must be integrated accurately for very long times and for a sufficiently large number of realizations of the ensemble. The inclusion of scattering needles with finite thickness and with spherical end caps provides some additional complexity in the implementation of the event-driven algorithm. Nevertheless, these obstacles can be surmounted with care, as indicated in the results of this work.

As the aspect ratio of scatterers increases, a change in both the diffusional and glassy dynamics of the system is observed. The observed aspect ratio dependence is visible in both the isotropic and nematic meshes. The nematic mesh shows larger displacements for all aspect ratios and both dynamical regimes when compared to an isotropic mesh. It is possible, however, that the idealized nematic mesh incorporated here, with near-perfect alignment, led to stronger anisotropy in the diffusion than would be accessible in the dynamics of a probe through an equilibrated, quickly quenched nematic. In unpublished work, however, we found that the dynamics of a probe through a mobile nematic array of spherocylinders continues to exhibit anisotropic diffusion, and this will be reported in detail elsewhere.

This model provides insight into the diffusive dynamics within liquid crystal environments such as those of apoferritin in *fd* virus.<sup>7–9</sup> Although hydrodynamic considerations have not been explicitly treated in the present work, the tracer size was seen to be central in determining the dynamical regime, as also seen in

the dynamics of apoferritin. It is, however, important to note that hydrodynamics plays a role in the overall dynamics of a tracer particle, as shown earlier by others through experiment and theory.<sup>32,33</sup> It would therefore be instructive to include hydrodynamic effects in future work.

There are also connections between the present model and that of a probe traversing through a porous gel or matrix of colloidal particles. The pore size or free volume available to the diffusing probe as well as geometric effects has been seen to affect the diffusion of the probe through the media.<sup>1,4,5,34–36</sup> The present work suggests that the geometry of the surrounding gel, that is, the formation of effective channels by the media versus a more isotropic orientation of free space, would greatly affect the diffusion through such media. The structural arrangement of scatterers gives rise to diffusion that is either correspondingly directed or isotropic. The possibility of such directed transport has also been observed in the dynamics of guest particles through a coiled pore system.<sup>37</sup> Indeed, in the coiled pore, two modes of diffusion are observed<sup>37</sup> and can be tuned by a modification of the coiled structure—that is, the relative ratio of the directed and isotropic structure in the static environment.

## AUTHOR INFORMATION

### Corresponding Author

\*E-mail: hernandez@gatech.edu.

## ACKNOWLEDGMENT

This work has been supported in part by the National Science Foundation through Grants Nos. NSF CHE 0749580 and CHE 0946869.

## REFERENCES

- (1) Vasanthi, R.; Ravichandran, S.; Bagchi, B. *J. Chem. Phys.* **2001**, *115*, 10022.
- (2) Schwanzer, D.; Coslovich, D.; Kurzidim, J.; Kahl, G. *Mol. Phys.* **2009**, *107*, 433.
- (3) Kim, K.; Miyazaki, K.; Saito, S. *Europhys. Lett.* **2009**, *88*, 36002.
- (4) Philipse, A.; Kluijtmans, S. *Physica A* **1999**, *274*, 516.
- (5) Kluijtmans, S.; Koenderink, G.; Philipse, A. *Phys. Rev. E* **2000**, *61*, 626.
- (6) Kurzidim, J.; Coslovich, D.; Kahl, G. *Phys. Rev. Lett.* **2009**, *103*, 138303.
- (7) Kang, K.; Gapinski, J.; Lettinga, M. P.; Buitenhuis, J.; Meier, G.; Ratajczyk, R.; Dhont, J. K. G.; Patkowski, A. *J. Chem. Phys.* **2005**, *122*, 044905.
- (8) Tao, Y.-G.; den Otter, W. K.; Padding, J. T.; Dhont, J. K. G.; Briels, W. J. *J. Chem. Phys.* **2005**, *122*, 244903.
- (9) Kang, K.; Wilk, A.; Buitenhuis, J.; Patkowski, A.; Dhont, J. K. G. *J. Chem. Phys.* **2006**, *124*, 044907.
- (10) Hershkovits, E.; Hernandez, R. *J. Chem. Phys.* **2005**, *122*, 014509.
- (11) F. Höfling, T. F.; Frey, E. *Phys. Rev. Lett.* **2006**, *96*, 165901.
- (12) Höfling, F.; Franosch, T. *Phys. Rev. Lett.* **2007**, *98*, 140601.
- (13) Höfling, F.; Frey, E.; Franosch, T. *Phys. Rev. Lett.* **2008**, *101*, 120605.
- (14) Ernst, M.; Weyland, A. *Phys. Lett.* **1971**, *34A*, 39.
- (15) Ernst, M.; Machta, J.; Dorfman, J.; Beijeren, v. H. *J. Stat. Phys.* **1984**, *34*, 477.
- (16) Machta, J.; Ernst, M.; Dorfman, J. *J. Stat. Phys.* **1984**, *35*, 413.
- (17) Bruin, C. *Physica* **1974**, *72*, 261.
- (18) Lewis, J. C.; Tjon, J. *Phys. Lett.* **1978**, *66A*, 349.
- (19) Chernov, N.; Dettmann, C. *Physica A* **2000**, *279*, 37.

- (20) Tucker, A. K.; Hernandez, R. *J. Phys. Chem. B* **2010**, *114*, 9628.
- (21) Tucker, A. K.; Hernandez, R. *J. Phys. Chem. B* **2011**, *115*, 4412.
- (22) Chang, R. W.; Jagannathan, K.; Yethiraj, A. *Phys. Rev. E* **2004**, *69*, 051101.
- (23) Jagannathan, K.; Sung, B. J.; Yethiraj, A. *Phys. Rev. Lett.* **2006**, *97*, 145503.
- (24) Sung, B. J.; Yethiraj, A. *J. Chem. Phys.* **2007**, *126*, 034704.
- (25) Höfling, F.; Munk, T.; Frey, E.; Franosch, T. *Phys. Rev. E* **2008**, *77*, 060904(R).
- (26) Hernandez, R.; Somer, F. L. *J. Phys. Chem. B* **1999**, *103*, 1064.
- (27) Hernandez, R.; Somer, F. L. *J. Phys. Chem. B* **1999**, *103*, 1070.
- (28) Hernandez, R. *J. Chem. Phys.* **1999**, *111*, 7701.
- (29) McGrother, S. C.; Williamson, D. C.; Jackson, G. *J. Chem. Phys.* **1996**, *104*, 6755.
- (30) Kim, I. C.; Torquato, S. *J. Chem. Phys.* **1992**, *96*, 1498.
- (31) Moreno, A.; Kob, W. *Europhys. Lett.* **2004**, *67*, 820.
- (32) Pagonabarraga, I.; Hagen, M.; Lowe, C.; Frenkel, D. *Phys. Rev. E* **1999**, *59*, 4458.
- (33) Kluijtmans, S. G.; Philipse, A. P. *Langmuir* **1999**, *15*, 1896.
- (34) Gong, J. P.; Hirota, N.; Kakugo, A.; Narita, T.; Osada, Y. *J. Phys. Chem. B* **2000**, *104*, 9904.
- (35) Dhara, D.; Chatterji, P. R. *J. Phys. Chem. B* **1999**, *103*, 8458.
- (36) Åkerman, B. *J. Phys. Chem. B* **1998**, *102*, 8909.
- (37) Stempniewicz, M.; Khalil, A.; Rohwerder, M.; Marlow, F. *J. Am. Chem. Soc.* **2007**, *129*, 10561.